



Minerva Access is the Institutional Repository of The University of Melbourne

Author/s:

Azhari, F;Davids, W;Chen, H;Ringer, SP;Wallbrink, C;Sterjovski, Z;Crawford, BR;Agius, D;Wang, CH;Schaffer, G

Title:

A Comparison of Statistically Equivalent and Realistic Microstructural Representative Volume Elements for Crystal Plasticity Models

Date:

2022-06-01

Citation:

Azhari, F., Davids, W., Chen, H., Ringer, S. P., Wallbrink, C., Sterjovski, Z., Crawford, B. R., Agius, D., Wang, C. H. & Schaffer, G. (2022). A Comparison of Statistically Equivalent and Realistic Microstructural Representative Volume Elements for Crystal Plasticity Models. *Integrating Materials and Manufacturing Innovation*, 11 (2), pp.214-229. <https://doi.org/10.1007/s40192-022-00257-4>.

Persistent Link:

<https://hdl.handle.net/11343/308231>

License:

CC BY



# A Comparison of Statistically Equivalent and Realistic Microstructural Representative Volume Elements for Crystal Plasticity Models

Fatemeh Azhari<sup>1,2,3</sup> · William Davids<sup>4,5</sup> · Hansheng Chen<sup>4,5</sup> · Simon P. Ringer<sup>4,5</sup> · Chris Wallbrink<sup>6</sup> · Zoran Sterjovski<sup>6</sup> · Bruce R. Crawford<sup>6</sup> · Dylan Agius<sup>6</sup> · Chun H. Wang<sup>2</sup> · Graham Schaffer<sup>1</sup>

Received: 23 November 2021 / Accepted: 27 February 2022 / Published online: 28 March 2022  
© The Author(s) 2022

## Abstract

Two methods used to construct a microstructural representative volume element (RVE) were evaluated for their accuracy when used in a crystal plasticity-based finite element (CP-FE) model. The RVE-based CP-FE model has been shown to accurately predict the complete tensile stress–strain response of a Ti–6Al–4V alloy manufactured by laser powder bed fusion. Each method utilized a different image-based technique to create a three-dimensional (3D) RVE from electron backscatter diffraction (EBSD) images. The first method, referred to as the realistic RVE (R-RVE), reconstructed a physical 3D microstructure of the alloy from a series of parallel EBSD images obtained using serial-sectioning (or slicing). The second method captures key information from three orthogonal EBSD images to create a statistically equivalent microstructural RVE (SERVE). Based on the R-RVEs and SERVEs, the CP-FE model was then used to predict the complete tensile stress–strain response of the alloy, including the post-necking damage progression. The accuracy of the predicted stress–strain responses using the R-RVEs and SERVEs was assessed, including the effects of each microstructure descriptor. The results show that the R-RVE and the SERVE offer comparable accuracy for the CP-FE purposes of this study.

**Keywords** Crystal plasticity · Finite element modelling · Statistically equivalent representative volume element · 3D-EBSD · Titanium · Laser powder bed fusion

## Introduction

Integrated computational materials engineering (ICME) is increasingly being used to fast-track materials innovation, qualification and integration. This requires modelling across scales, from the atomic to the continuum, to predict a material's mechanical properties using the composition, processing conditions, and microstructural features as input variables, which can then be used for design and testing purposes. Such capability requires the coupling of micro-mechanics models with representative volume elements (RVEs) that represent the material's microstructure. Azhari et al. [1] recently developed a crystal plasticity-based finite element (CP-FE) model to predict the complete tensile stress–strain response of the laser powder bed fusion (L-PBF) Ti–6Al–4V alloy using an RVE to capture the essential attributes of its microstructure. This material is anisotropic and inhomogeneous, which has a major effect on its plastic deformation and failure. The CP-FE model developed by Azhari et al. [1] is similar to many other CP-FE models that have been developed to predict the mechanical response of titanium alloys from

✉ Fatemeh Azhari  
fatemeh.azhari@monash.edu

<sup>1</sup> Department of Mechanical Engineering, The University of Melbourne, Melbourne, VIC 3010, Australia

<sup>2</sup> School of Mechanical and Manufacturing Engineering, University of New South Wales, Sydney, NSW 2052, Australia

<sup>3</sup> Department of Civil Engineering, Monash University, Melbourne, VIC 3800, Australia

<sup>4</sup> Australian Centre for Microscopy and Microanalysis, The University of Sydney, Sydney, NSW 2006, Australia

<sup>5</sup> School of Aerospace, Mechanical and Mechatronic Engineering, The University of Sydney, Sydney, NSW 2006, Australia

<sup>6</sup> Aerospace Division, Defence Science and Technology Group, 506 Lorimer Street, Fishermans Bend, Vic 3207, Australia

their microstructure [2–25]. Uniquely, it also includes crack band theory [26] to minimize mesh sensitivity.

It is critically important that the RVE describes the three-dimensional (3D) microstructural characteristics such as grain shape, grain size, crystallography, and anisotropy. Other researchers have used a quasi-3D RVE [13, 14], a hypothetical RVE [15–17], or a statistically equivalent RVE (SERVE). The SERVE can be constructed from two-dimensional (2D) or 3D statistical information obtained from the microstructure and may be used to evaluate accurate homogenized properties of the material [27]. A common technique for constructing the SERVE is to use the microstructure statistics obtained from three orthogonal 2D electron backscattered diffraction (EBSD) images [18–23]. For example, the quasi-3D RVE in Ref. [14] is a cube of 95  $\mu\text{m}$  sides and 8  $\mu\text{m}$  thickness generated from a 2D EBSD scan of a dual-phase L-PBF Ti–6Al–4V alloy. The hypothetical RVE used in Ref. [15] was based on the grain size distribution and  $\alpha$  grain fraction obtained from optical micrographs and included randomly oriented  $\alpha$  grains. Monte Carlo sampling was used to represent the scatter in the material microstructure.

The model described by Azhari et al. [1] uses a SERVE constructed from three orthogonal 2D EBSD images. This contains information on the critical grain statistics, including the crystalline structures of the constituent phases, the grain aspect ratio, the grain size distribution, the orientation distribution functions (ODFs), and the axis ODFs representing the crystallographic and morphological orientations of the grains. Thus, the SERVE is visually different from but statistically equivalent to the real microstructure. However, the accuracy of the SERVE for use in a CP-FE model was not tested in Ref. [1]. For this purpose, an alternative method for obtaining the RVE was developed by constructing the microstructure in 3D from serial sectioning, denoted here as a realistic RVE (R-RVE). This R-RVE captures the exact heterogeneous polycrystalline grain characteristics of the titanium alloy [24, 25]. While accurate, the R-RVE method requires specialized equipment such as a focused ion beam scanning electron microscope (FIB-SEM) and the data are time-consuming and expensive to collect. Because the SERVE is derived from three orthogonal 2D images, its collection requires less device time than is required for serial sectioning, although the time for sample preparation is longer.

The objective of this study is to assess the relative accuracy of the calculated stress–strain curves of two stress-relieved and annealed samples of the L-PBF Ti–6Al–4V alloy using the SERVE and an R-RVE in CP-FE modelling.

## Acquisition of Experimental Data and RVE Development

Two pairs of the annealed L-PBF Ti–6Al–4V cylindrical bars were fabricated. Strain-controlled tensile tests were carried out on standard cylindrical tensile specimens machined from one of the bars within each pair. For the microstructural characterization required to develop the RVEs, 3-mm-thick discs with diameter of 10 mm were sectioned from the second bar within each pair. The two bars within each pair were taken from adjacent locations on the build plate to ensure the similarity of their microstructure. However, the test regions between pairs were from different build heights to enable the validation of the model. Fabrication and testing of the bars were described in Ref. [1]. The following sections will present the methods used to create the SERVEs and R-RVEs.

### Statistically Equivalent RVE (SERVE)

The SERVE is a statistical model that does not reproduce the actual lath-shaped microstructure but incorporates the key microstructure statistics, including the crystalline structures of the constituent phases, the grain size distribution, the crystallographic and morphological orientations, and the mean aspect ratio of the grains. To capture the 3D characteristics of the microstructure, the SERVE was developed from three orthogonal 2D EBSD microstructural scans with two scans taken parallel to the build plate direction and the third scan taken normal to the build direction. A schematic drawing of the disc extracted from the annealed L-PBF Ti–6Al–4V specimen and three orthogonal disk surfaces used for EBSD imaging is shown in Fig. 1. These quarter disc samples were first embedded in epoxy resin and then ground and polished using a Struers Tegramin-30 Auto-polishing machine. The samples were ground with 500 Grit (US #360) silicon carbide paper, polished with 9  $\mu\text{m}$  and 1  $\mu\text{m}$  diamond suspension, and finished with oxide polishing suspension. The 2D EBSD scans were collected from the red solid surfaces shown in Fig. 1b–d using an FEI Quanta 3D FIB-SEM machine equipped with an EDAX Hikari EBSD detector. The EBSD data were collected at an accelerating voltage of 15 kV, a probe current of 11 nA, a working distance of 15 mm and a step size of 100 nm. Collecting the three 2D EBSD scans consumed approximately 2–3 h of the instrument time. The microstructural analysis was repeated for the second sample.

The orthogonal EBSD scans (dimension  $\sim 70 \times 70 \mu\text{m}^2$ ) collected from Specimens 1 and 2 are presented in Fig. 2.

The 3D SERVE was generated based on a range of morphological and crystallographic parameters describing the microstructure, which were extracted from the orthogonal EBSD scans illustrated in Fig. 2. To this end, the

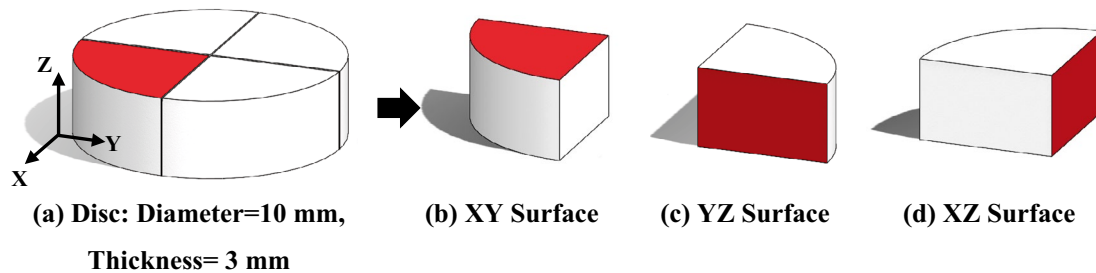


**Fig. 1** Schematic of the three orthogonal disk surfaces used for EBSD imaging. The solid red surfaces were those examined [1]

DREAM.3D® software [28] was first used to assign feature identification numbers (IDs) to the grains in each 2D EBSD scan. The grains were segmented by grouping neighbouring voxels with similar crystallographic orientations. Then the key microstructural descriptors, including the crystalline structures of the constituent phases, the grain aspect ratio, the grain size distribution, the orientation distribution functions (ODFs), and the axis ODFs datasets representing the crystallographic and morphological orientations of the grains, were extracted from the grains identified (segmented) in the 2D EBSD scans. The original EBSD scans indicated that the specimen might also contain up to 1 vol. %  $\beta$  phase. However, because this low volume fraction of the  $\beta$  phase does not substantially alter the stress state at the  $\alpha$  phase [25], a fully  $\alpha/\alpha'$  hexagonal close packed (HCP) microstructure was assumed for generating the 3D SERVE. The 3D size and aspect ratio distributions of the grains in the 3D SERVE were estimated using stereological projections [29]. The surface crystallographic orientation and misorientation distribution functions were directly used for creating 3D crystallographic distributions [29]. A log-normal distribution was assumed for the grain sizes [30, 31], meaning that the probability density function (PDF) of the equivalent spherical diameter (ESD) of each crystallite is defined as:

$$\text{PDF}(ESD) = \frac{1}{(ESD)\sigma\sqrt{2\pi}} \exp\left(-\frac{(\ln ESD - \mu)^2}{2\sigma^2}\right) \quad (1)$$

in which  $\mu$  and  $\sigma$  are the mean and standard deviation on the log-scale, respectively.

To construct the SERVE, a series of customizable pipelines shown in Fig. 14 of the Appendix were used. The  $16 \times 16 \times 16 \mu\text{m}^3$  3D SERVEs generated from the annealed L-PBF Ti–6Al–4V specimens 1 and 2 (labelled as SERVE 1 and 2, respectively) are illustrated in Fig. 3. The accuracy of the technique used for construction of the SERVE was previously validated in Ref. [1]. As explained in Ref. [1], the SERVE is a statistical model and does not represent the actual lath-shaped microstructure. The grains represented by the SERVE are elongated and not equiaxed, but their mean

aspect ratio is equal to that of the actual microstructure. Crystallographic and morphological orientations obtained from the EBSD scans were randomly assigned to the grains of the SERVEs. These are limitations of the SERVE generation method, which may affect the predicted mechanical response for certain loading conditions; however, it will be shown in "Comparison of the Experimental and Calculated Stress–Strain Results" section that they lead to accurate tensile stress–strain response for the annealed L-PBF Ti–6Al–4V alloy considered in this study. The microstructure data including grain sizes and orientations are presented in detail in Ref. [1] and therefore not repeated here.

### Realistic RVE (R-RVE)

The R-RVEs were constructed from a series of parallel 2D EBSD images obtained by automated serial sectioning. A section parallel to the top XY plane (Fig. 1b) was cut from the quarter disc and mechanically polished to  $\sim 60 \mu\text{m}$  thickness, before being mounted onto a pre-tilted holder at  $70^\circ$ . Multiple parallel EBSD images were then captured by automated serial sectioning using a dual-beam FEI Helios Xe<sup>+</sup> Plasma FIB-SEM microscope. The specimens were sliced with an accelerating voltage of 12 kV and a current of 5 nA. A 200 nm step size was selected. The total milling time for each slice was between 3 to 5 min. The sectioned slices were coated with a Pt protection layer to minimize curtaining effects. The EBSD data were obtained using an Oxford Symmetry detector and Aztec 4.2 software with an accelerating voltage of 20 kV and beam current of 3.2 nA. The process was automated using the FEI Auto Slice and View software. The total acquisition time was 34 h for Specimen 1 and 63 h for Specimen 2. From the resultant series of 3D EBSD scans (a non-right prism), the R-RVEs with dimensions of  $34 \times 34 \times 16 \mu\text{m}^3$  (Specimen 1) and  $40 \times 25 \times 25 \mu\text{m}^3$  (Specimen 2) were constructed.

Examples of 2D EBSD slices obtained from the annealed L-PBF Ti–6Al–4V tensile specimens by the serial sectioning technique are shown in Fig. 4. The 3D EBSD scans were transferred to DREAM.3D and the reconstruction of 3D data

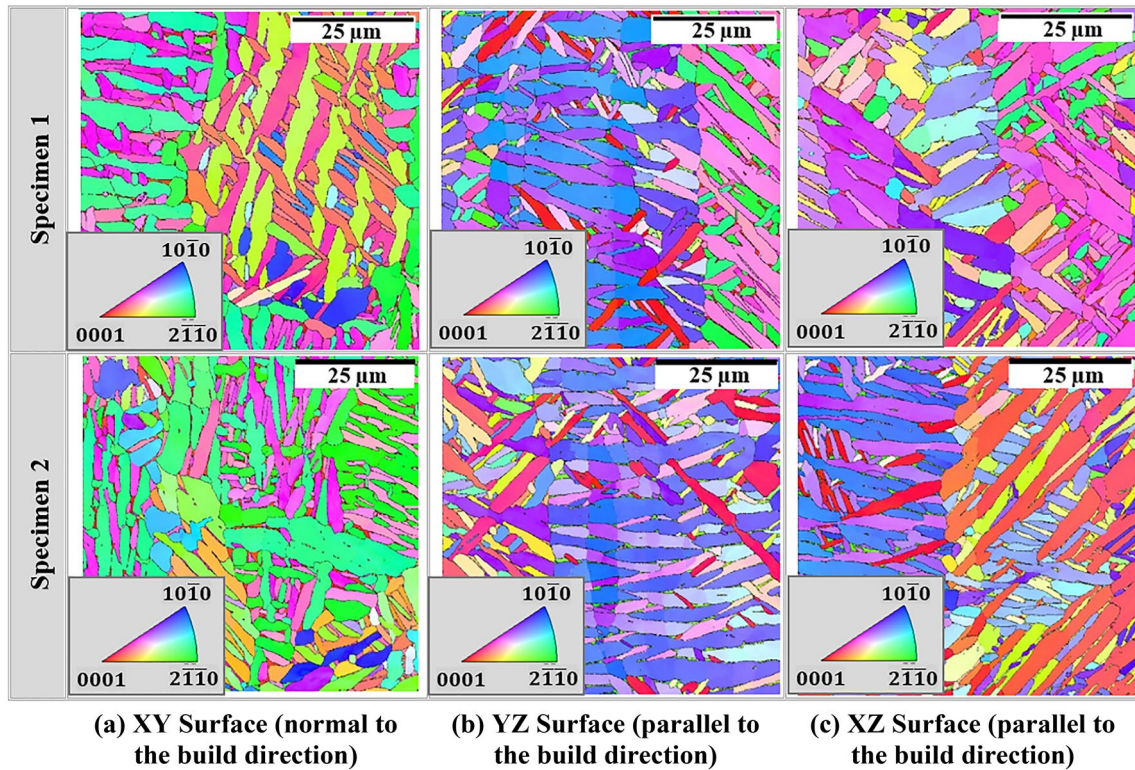
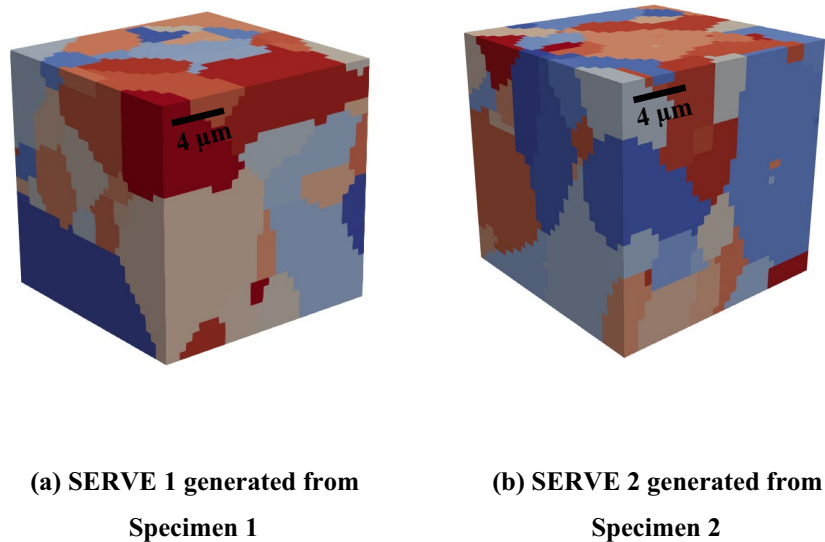


**Fig. 2** Illustration of the three orthogonal EBSD scans obtained from the annealed L-PBF Ti–6Al–4V specimens, after [1]

**Fig. 3** The 3D SERVE ( $16 \times 16 \times 16 \mu\text{m}^3$ ) constructed using three orthogonal EBSD scans obtained from the annealed L-PBF Ti–6–4 tensile specimens [1]. Color of the grains represents their feature IDs (i.e. grain number)



was performed through certain series of customizable pipelines (shown in Fig. 15 of the Appendix) indexing all grains [28]. The 3D R-RVEs ( $16 \times 16 \times 16 \mu\text{m}^3$ ) constructed from the 3D EBSD scans of Specimens 1 and 2 are presented in Fig. 5. The microstructure of both specimens consists

largely of  $\alpha$  laths arranged in a basket-weave morphology. The grains can either be equiaxed, needle-like, or plate-like shape in form. The total number of  $\alpha$  laths fully encapsulated within R-RVEs 1 and 2 is 91 and 119, respectively.

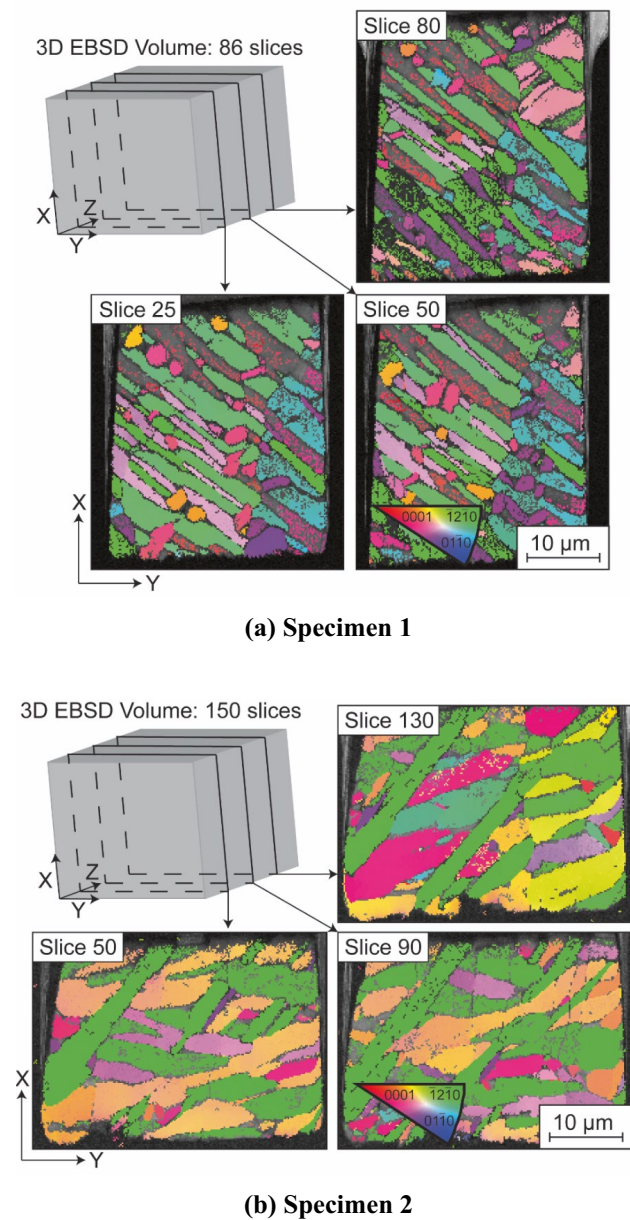


Fig. 4 Examples of 2D EBSD slices obtained from the annealed L-PBF Ti-6-4 tensile specimens by the serial sectioning technique

### CP-FE Model

#### Crystal Plasticity Model

Complete details of the constitutive equations used in the CP-FE model were described in Ref. [1]. This section provides a summary of these equations, which define the slip rate as a function of stress and the microstructural state of the material.

The slip rate ( $\dot{\gamma}^\alpha$ ) was defined by a viscoplastic power-law [32] as a function of the resolved shear stress ( $\tau^\alpha$ ), the material’s resistance to slip ( $g^\alpha$ ) on the  $\alpha$ -th slip system, and

$\dot{\gamma}_0$  and  $m$  material parameters which represent the reference slip rate and the strain rate sensitivity, respectively [33]. The initial value of  $g^\alpha$  (i.e.  $g^\alpha(0)$ ) is assumed to be equal to the initial critical resolved shear stress on the  $\alpha$ -th slip system ( $\tau_0$ ). The evolution of  $g^\alpha$  over time is described in terms of the slip hardening moduli due to self and latent hardenings. The latent hardening moduli ( $h_{\alpha\beta}$  where  $\alpha \neq \beta$ ) is used to capture the interactions between different slip systems, and the self-hardening moduli ( $h_{\alpha\alpha}$ ) captures the hardening evolution on a single slip system. The  $h_{\alpha\beta}$  moduli are related to  $h_{\alpha\alpha}$  by a material constant ( $q$ ), i.e.  $h_{\alpha\beta} = qh_{\alpha\alpha}$ , where  $h_{\alpha\alpha}$  is defined by the equations proposed by Peirce et al. [34] and Asaro [35] in terms of the initial hardening modulus ( $h_0$ ), the saturation value of flow stress on the  $\alpha$ -th slip system ( $\tau_s$ ), and the Taylor cumulative shear strain on all slip systems ( $\gamma$ ). The effect of  $\alpha'$ /α colony size on the plastic deformation is considered using the Hall–Petch relation [36] which calculates  $\tau_0$  in terms of a Hall–Petch slope ( $K_y$ ), the grain ESD, and a constant which is independent of the grain size ( $\tau_\infty$ ).

The damage accumulation in the material was incorporated using a model proposed by Kim and Yoon [37]. It is a continuum damage model which allows us to consider the necking of the material by introducing stiffness degradation into the CP-FE model. The model assumes that damage is initiated once the maximum shear strain during the CP-FE simulation reaches a critical value. A damage ( $D$ ) parameter is included in the calculation of the Cauchy stress tensor ( $\sigma(\epsilon)$ ) as:

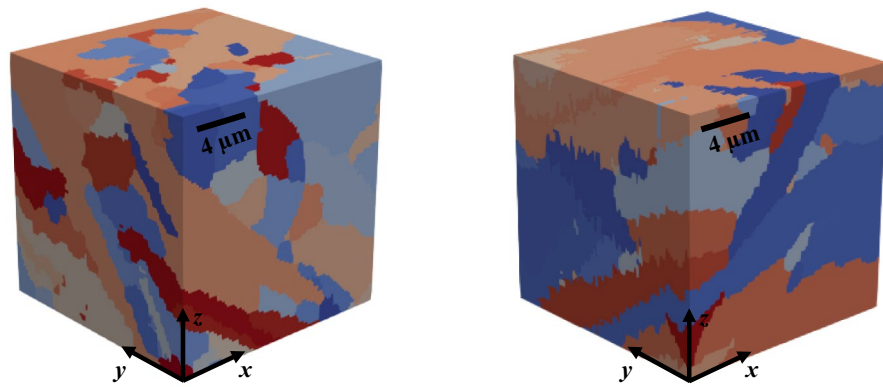
$$\sigma(D, \epsilon) = (1 - D) \cdot \sigma(\epsilon) \tag{2}$$

where  $D$  is calculated in terms of the maximum shear strain ( $\gamma_m$ ), which is a state variable calculated at each time increment of the simulation using Eq. (3).

$$D = \begin{cases} 0 & \gamma_m \leq \gamma_{mf,ini} \\ \frac{D_{max}}{(\gamma_{mf,max} - \gamma_{mf,ini})^M} (\gamma_m - \gamma_{mf,ini})^M & \gamma_{mf,ini} < \gamma_m < \gamma_{mf,max} \\ D_{max} & \gamma_{m,max} \leq \gamma_m \end{cases} \tag{3}$$

Damage evolution is influenced by  $\gamma_{mf,ini}$  and  $\gamma_{mf,max}$ , which represent the maximum shear strain at which damage initiates and reaches the maximum value  $D_{max}$ , respectively. The extent of damage evolution is controlled by an exponent ( $M$ ). The parameters of the damage model were calibrated using the experimental stress–strain data obtained from physical tensile testing. A modified crack-band theory described in [1] was used to eliminate the mesh-sensitivity of the predicted failure strain.

**Fig. 5** The 3D R-RVEs ( $16 \times 16 \times 16 \mu\text{m}^3$ ) constructed from the 3D EBSD scans obtained from the annealed L-PBF Ti-6–4 tensile specimens by the serial sectioning technique. Color of the grains represents their feature IDs (i.e. grain number)



**(a) R-RVE 1 generated from Specimen 1 (b) R-RVE 2 generated from Specimen 2**

**Table 1** Boundary conditions considered for the RVE, where  $\Theta$ : rotation and  $U$ : displacement

Surface	Boundary condition	Description
Bottom surface	ZSYMM	$\Theta_x = \Theta_y = U_z = 0$
Left surface	YSYMM	$\Theta_x = \Theta_z = U_y = 0$
Back surface	XSYMM	$\Theta_y = \Theta_z = U_x = 0$
Top surface	Loading	$U_z$ is a ramp function (maximum value = 2.5 mm)
Front surface	Free	
Right surface	Free	

## FE Implementation

The described constitutive equations were applied for HCP crystals through a FORTRAN user-defined material subroutine (UMAT) based on the subroutine initially written by Huang [38] for cubic crystals in a continuum framework. The UMAT code enabled activation of all families of slip systems for HCP crystals, including three basal, three prismatic, 12 pyramidal  $\langle c + a \rangle$  and six pyramidal  $\langle a \rangle$  slip systems. The developed UMAT subroutine was linked with the ABAQUS/Standard [39] FE code. During the CP-FE simulation, the stresses, strains and the solution-dependent state variables at each timeframe were updated. The nonlinear equations were solved using an iterative Newton–Raphson solution technique.

The RVE boundary conditions were chosen by assuming symmetry based on the suggestions made in Refs. [40, 41] (Table 1). A ramp displacement was applied to the top surface of the RVE, the front and right surfaces were stress-free, and constrained boundary conditions were applied to the other three surfaces (the bottom, left, and back surfaces) to impose symmetry.

The global stress–strain response of the RVE was calculated using a Python script that homogenizes the local

stress and strain values at the integration points of the elements (obtained from the CP-FE simulation) over the RVE volume [42].

## Calibration of the CP Model Parameters

The room temperature elastic constants ( $C_{ij}$ ), which control the elastic evolution of the L-PBF Ti–6Al–4V alloy, were adopted from Ref. [14] in which semi-3D CP-FE simulation of an L-PBF Ti–6–4 was performed. The symmetry of the HCP crystal structure [43] suggests that  $C_{11} = C_{22}$ ,  $C_{13} = C_{23}$ ,  $C_{44} = C_{55}$ , and  $C_{66} = (C_{11} - C_{12})/2$ ; therefore, only six independent elastic constants were defined.

The parameters related to the plastic deformation and damage evolution of the material were calibrated based on the experimental stress–strain curve. Following the details presented in "Crystal Plasticity Model" section, the specific parameters calibrated were:

- Slip hardening parameters:  $h_0$  (MPa),  $\tau_\infty$  (MPa),  $\tau_s$  (MPa) and  $q$
- Strain rate sensitivity parameters:  $m$  and  $\dot{\gamma}_0$  ( $s^{-1}$ )
- Hall–Petch relation parameter:  $K_y$  ( $\text{MPa}\sqrt{\text{mm}}$ )
- Damage evolution parameters:  $\gamma_{mf,ini}$ ,  $\gamma_{mf,max}$ ,  $M$  and  $D_{max}$

Details of the calibration process and the final set of calibrated CP parameters listed above are given in Ref. [1].

## Integrating the RVEs and the CP-FE Model

The output RVEs generated from the DREAM.3D pipelines are a grid of voxels with a grain number and a set of ODFs assigned to each voxel. A MATLAB script was developed to prepare the generated RVEs for the CP-FE simulation and discretize them into eight-node linear brick ABAQUS elements (C3D8).

The meshed RVEs (i.e. SERVEs and R-RVEs) generated from Specimens 1 and 2 and prepared for the CP-FE simulation are illustrated in Fig. 6. These are the SERVEs and the R-RVEs shown in Figs. 3 and 5 and meshed with  $64 \times 64 \times 64$  C3D8 elements (elements length =  $0.25 \mu\text{m}$ ). The orange arrows are the tensile displacement load, and the blue-orange supports represent the XSYMM, YSYMM, and XSYMM boundary conditions [39].

## Results and Discussion

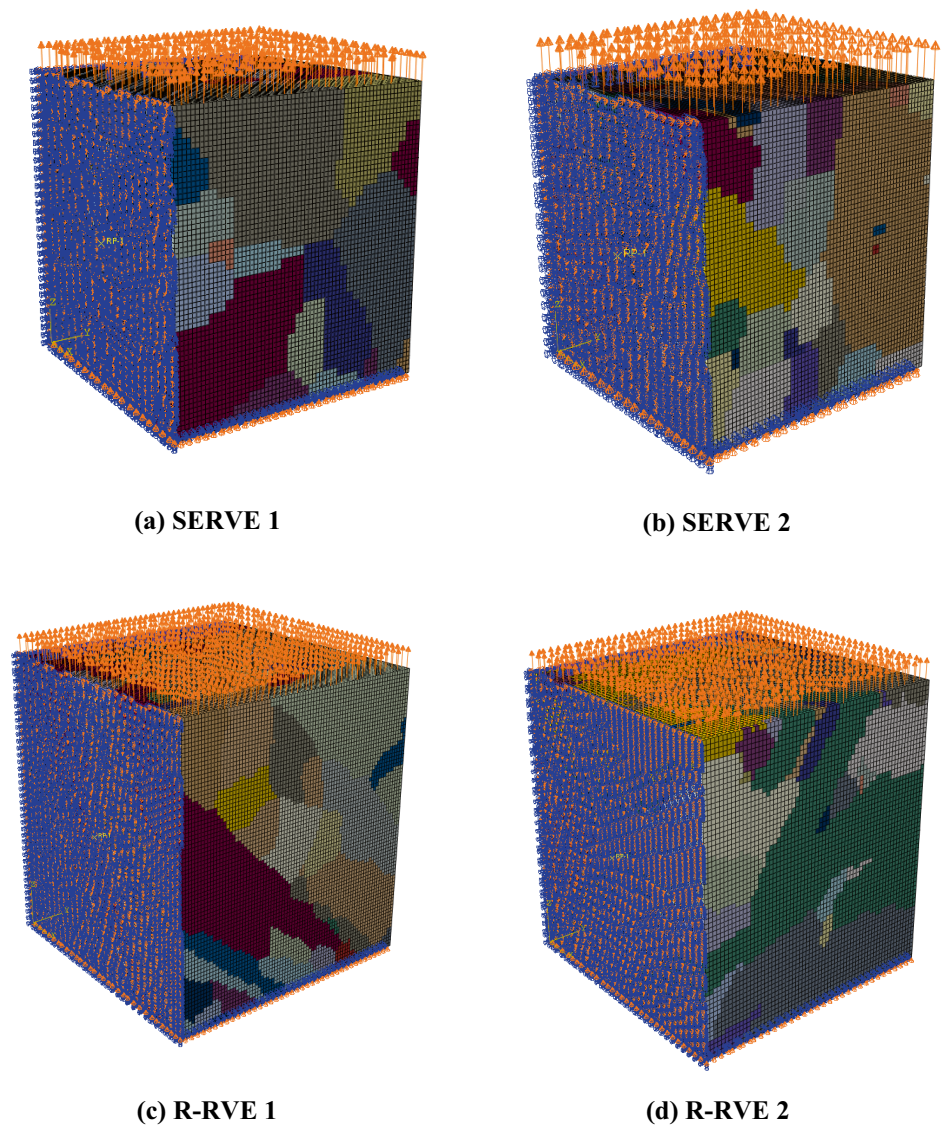
A comparison study was performed on the grain statistics of the SERVEs and the R-RVEs and the corresponding predicted stress–strain responses. The outcome of the two comparison studies was then compared to examine the effect of

each microstructural characteristic on the accuracy of the homogenized results obtained from the CP-FE simulations.

### Comparison of the Grain Statistics in the Developed RVEs

The first microstructural characteristic is the distribution of the grain size. As mentioned in "Statistically Equivalent RVE (SERVE)" section, the grain sizes have a log-normal distribution [30, 31], suggesting that the logarithm of the equivalent spherical diameter of each crystallite is normally distributed within the microstructure with the log-normal PDF defined in Eq. (1). For each specimen, the log-normal PDFs of ESD in the SERVE and the R-RVE are compared in Fig. 7. Values of  $\mu$  and  $\sigma$  (the log-normal mean and standard deviation) for each RVE are presented in the legend of these plots. The data presented in Fig. 7 show that the grain size

**Fig. 6** Illustration of the meshed RVEs prepared for the CP-FE simulation. The orange arrows represent the displacement load and the blue-orange supports represent the XSYMM, YSYMM and XSYMM boundary conditions explained in Table 1



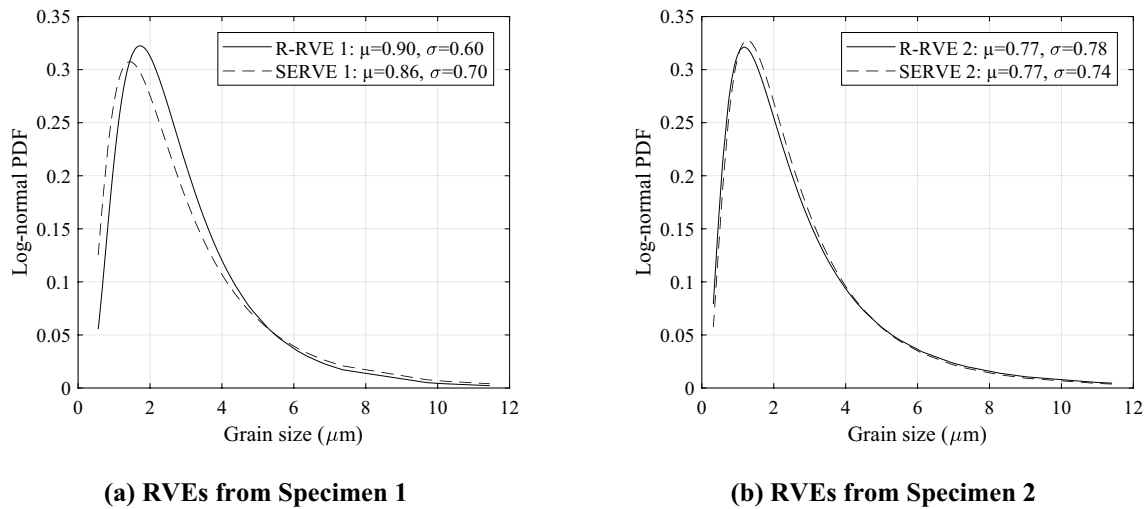


**Fig. 7** Comparison of the PDFs of the equivalent grain size of the SERVEs and the R-RVEs constructed from Specimens 1 and 2 (a and b)

distribution of the R-RVE and the SERVE closely match. The values of  $\mu$  for the grain size in the R-RVEs and the SERVEs are similar. However, the difference between the  $\sigma$  for the grain size in the R-RVEs and the SERVEs is  $\sim 14\%$  and  $\sim 6\%$  for Specimens 1 and 2, respectively.

A second microstructural characteristic considered is the average misorientation angle between a grain and all neighbouring grains. The average misorientation angles are divided into bins with  $2^\circ$  length, and the frequency distribution curves of the average misorientation angle for the R-RVEs and the SERVEs generated from Specimens 1 and 2 are compared in Fig. 8. The vertical axis in Fig. 8, i.e. frequency (%), shows the percentage of each average

misorientation angle in the RVE. Figure 8 indicates that the average misorientation angle with maximum frequency (i.e. repeated the most) in the R-RVE and the SERVE is very close for both Specimens 1 and 2, i.e. close to  $60^\circ$  for all RVEs. The ranges of the misorientation angles for the R-RVE and the SERVE generated from each specimen have less than  $7^\circ$  difference.

### Comparison of the Experimental and Calculated Stress–Strain Results

Stress–strain curves and mechanical properties from the CP-FE simulations and the experimental results are

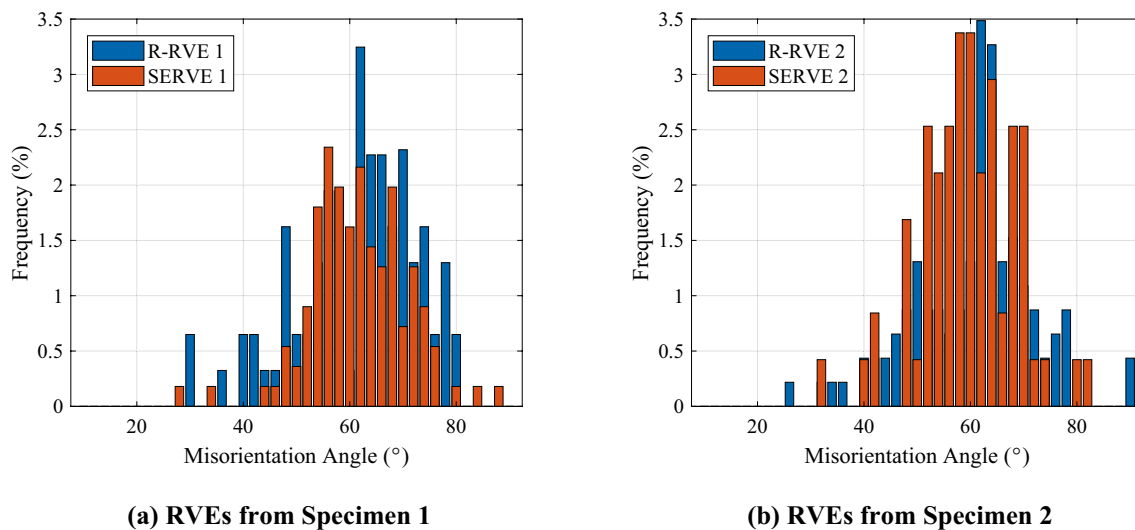


**Fig. 8** Comparison of the frequency distribution of the average misorientation angle between the feature and all contacting features of the SERVEs and the R-RVEs constructed from Specimens 1 and 2 (a and b)

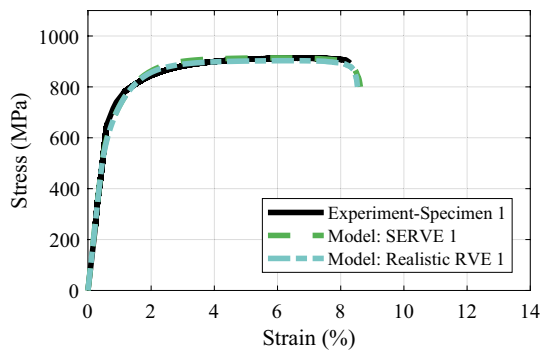
compared in Fig. 9. The CP parameters given in Ref. [1] were used for the CP-FE simulation of all RVEs. However, these parameters were only calibrated for SERVE 1; other RVEs were used to validate the CP-FE model. Engineering stress–strain data were used because the model considers necking in the region beyond the ultimate tensile stress. Localized necking due to nucleation and growth of microvoids was not modelled [44]. There is a close match between the calculated and experimental curves for both specimens and for both the R-RVE and the SERVE.

The consistency in the monotonic tensile simulation results using this approach to construct a SERVE was analysed by generating seven additional SERVEs using the same morphological and crystallographic statistics in each case, labelled as SERVE 1-*i*, *i* = 1–7. This was done to test the variance in simulation results due to the changing grain environments in each SERVE as a consequence of the random sampling from each of the microstructure feature distributions. The homogenized stress–strain responses obtained from CP-FE simulations on SERVE 1–1 to 1–7 were compared to simulation outputs from R-RVE 1 and SERVE 1, and Specimen 1 experimental results in Fig. 10. This figure indicates that there is little discernible difference between all these simulations and the experimental results.

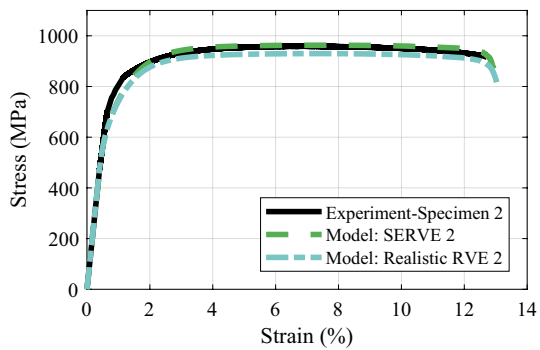
The 0.2% proof stress ( $f_{0.2}$ ), the ultimate tensile strength ( $f_u$ ) and the failure strain ( $\epsilon_f$ ) were extracted from each of these predicted stress–strain curves. Figure 11a shows the errors in these mechanical parameters with respect to the experimental values:

$$\text{error (\%)} = \left( \frac{p^{\text{Model}} - p^{\text{Experiment}}}{p^{\text{Experiment}}} \right) \times 100 \quad (4)$$

where *p* is the mechanical parameter (i.e.  $f_{0.2}$ ,  $f_u$ , or  $\epsilon_f$ ) of interest. For improved visualization of the mechanical parameters predicted by the additional SERVEs, mean



(a) Specimen 1



(b) Specimen 2

**Fig. 9** Global stress–strain curves from CP-FE simulations on SERVE 1 and 2, R-RVE 1 and 2, and experimental test. SERVE 1/Specimen 1 was used for calibration and SERVE 2/Specimen 2 was used for validation. **a** SERVE 1 and R-RVE 1, **b** SERVE 2 and R-RVE 2

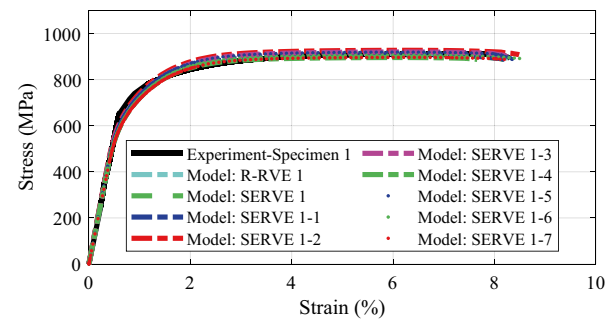


**Fig. 10** Homogenized stress–strain curves from CP-FE simulations on R-RVE 1, SERVE 1, SERVE 1–1 to 1–7, and experimental test on Specimen 1

values (red marker) and box plots [45] indicating the 25th and 75th percentiles are also presented in Fig. 11b.

The maximum relative error (%) for each of the serves was calculated as ~4% for  $f_{0.2}$ , ~3% for  $\epsilon_f$ , and ~2% for  $f_u$  with respect to the experimental values. Therefore, little variance was observed in the simulations using SERVEs constructed from microstructural data obtained using three orthogonal 2D slices.

The robustness of this approach can be further investigated by applying it to the R-RVE 1. If the approach to extracting vital microstructural data to construct a SERVE is robust, then the simulation results obtained from SERVEs constructed from data obtained from three orthogonal faces extracted from the R-RVE 1 should reproduce the monotonic simulation results achieved by the R-RVE 1.

Orthogonal 2D slices were extracted from R-RVE 1, with the locations of the extracted slice illustrated in Fig. 12. Eight SERVEs were created from random orthogonal slices (Table 2) which are labelled as SERVE Ri, *i* = 1–8. Multiple SERVEs were generated to investigate the variance in the simulation results.

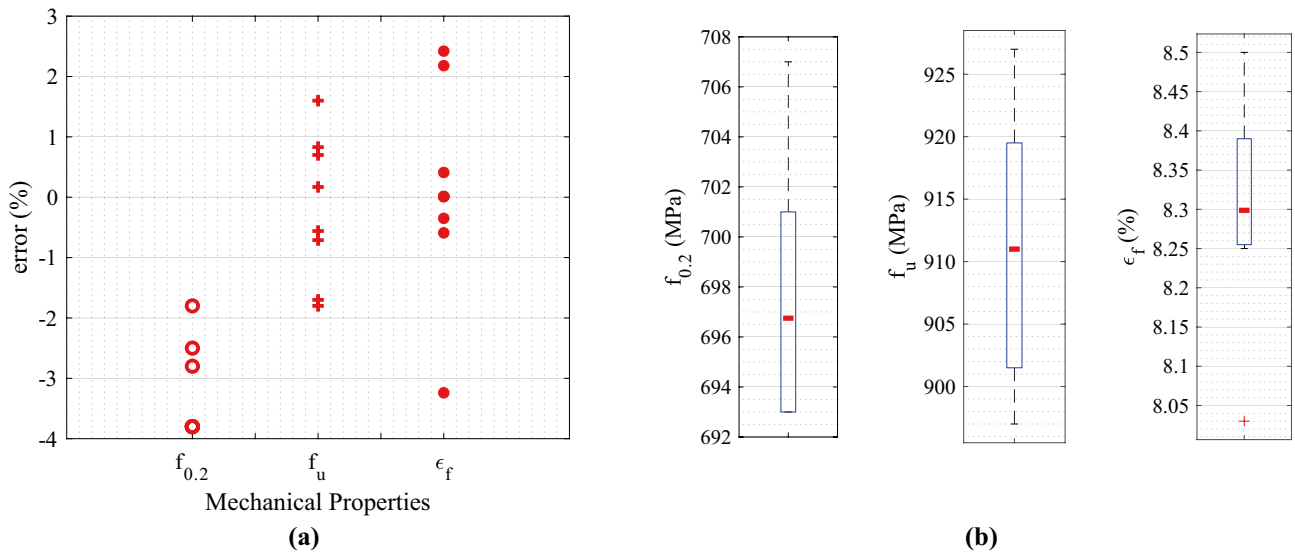


**Fig. 11** **a** variation of the relative error (%) of the predicted mechanical parameters with respect to the experimental values; and **b** box plots (indicating the 25th and 75th percentiles) and mean values (red marker) of the predicted mechanical parameters predicted for SERVE

1 and SERVE 1–1 to 1–7. The red cross marker corresponds to the and outlier in the predictions of  $\epsilon_f$ , which is outside 1.5 times the interquartile range

The homogenized stress–strain responses obtained from CP-FE simulations on these additional SERVEs (SERVE R1 to R8) were compared to those obtained from CP-FE simulations on R-RVE 1, SERVE 1 and experimental test on Specimen 1 in Fig. 13a. This figure shows consistency among the modelled stress–strain results of the additional SERVEs (SERVE R1 to R8), SERVE 1, R-RVE 1, and the experimental stress–strain results. Using Eq. (4), the relative error for each of the simulation results using the generated SERVEs was calculated and provided in Fig. 13b. The results show that a maximum error (%) of ~3% for  $f_{0.2}$  and ~3.5% for both  $f_u$  and  $\epsilon_f$  exists, with most SERVEs predicting mechanical properties with less than 2.2% error with respect to the experimental values. The spread in mechanical properties is shown using box plots in Fig. 13c.

The similar spread in simulation results seen in Fig. 11 and Fig. 13 shows the viability of the three orthogonal surface approach to extracting robust morphological and crystallographic statistics. Extracting data obtained from three orthogonal 2D slices provides enough vital information on the crystallographic and morphological characteristics to construct SERVEs representative of the microstructure for the purposes of CP-FE modelling of tensile behaviour.

### Summary and Conclusions

A comparison study was performed for application of a statistically equivalent RVE (SERVE) and a realistic RVE (R-RVE) in the CP-FE simulation of complete tensile

loading (until failure) of the annealed L-PBF Ti–6Al–4V alloys. A 3D SERVE, which is statistically equivalent to the actual polycrystalline microstructure, and an R-RVE, which captured the heterogeneous polycrystalline grain characteristics inherent in the material, were generated for each of the two different annealed L-PBF Ti–6Al–4V specimens. One of the SERVEs was used for calibration of the CP-FE model parameters while the other RVEs were used for validation of the model. CP-FE simulations were conducted on the generated RVEs, and their complete stress–strain responses were calculated. The statistics of the microstructure grains in the SERVEs and the R-RVEs were compared. Also, the predicted stress–strain responses of the generated RVEs were compared to the experimental curves.

**Table 2** SERVEs created from the 2D slices extracted from R-RVE 1 along three orthogonal planes which are shown and labelled in Fig. 12

SERVE label	Slice parallel to the xy plane	Slice parallel to the xz plane	Slice parallel to the yz plane
SERVE R1	Slice xy1	Slice xz2	Slice yz3
SERVE R2	Slice xy3	Slice xz1	Slice yz4
SERVE R3	Slice xy4	Slice xz3	Slice yz1
SERVE R4	Slice xy1	Slice xz1	Slice yz1
SERVE R5	Slice xy4	Slice xz4	Slice yz4
SERVE R6	Slice xy2	Slice xz3	Slice yz2
SERVE R7	Slice xy3	Slice xz1	Slice yz3
SERVE R8	Slice xy4	Slice xz2	Slice yz2

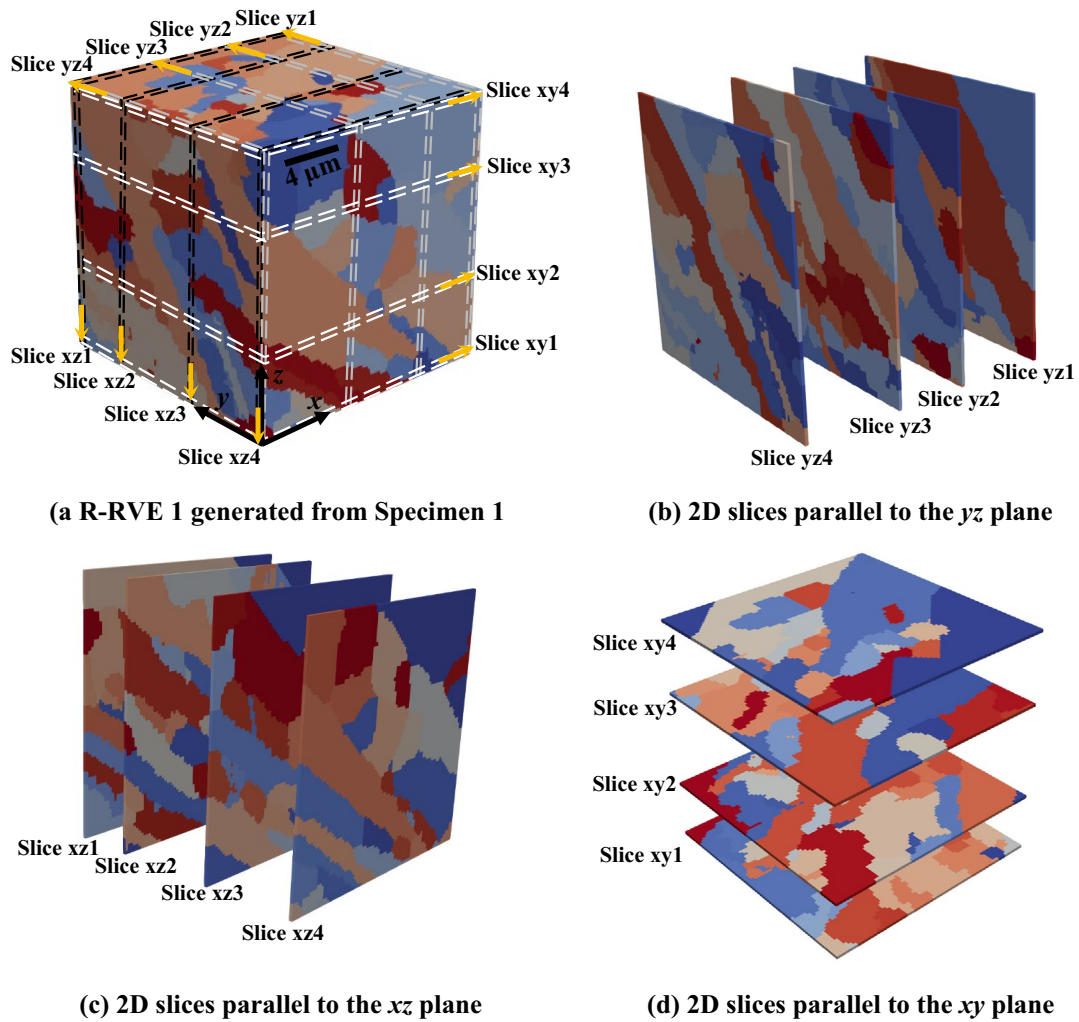
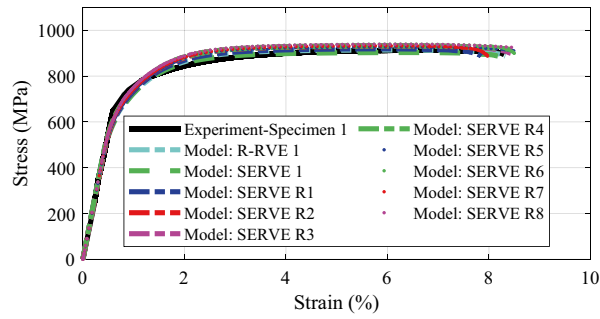
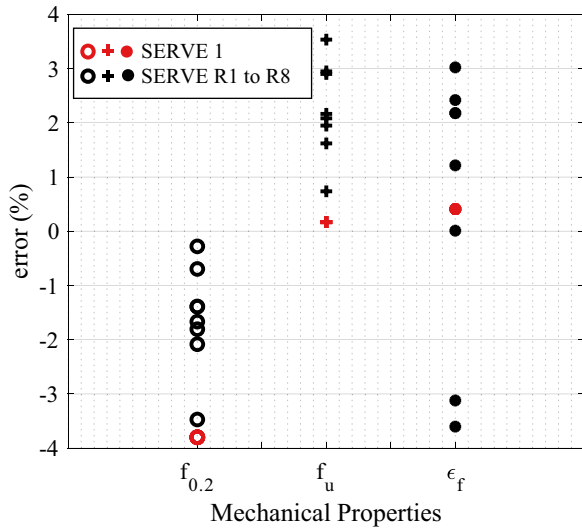


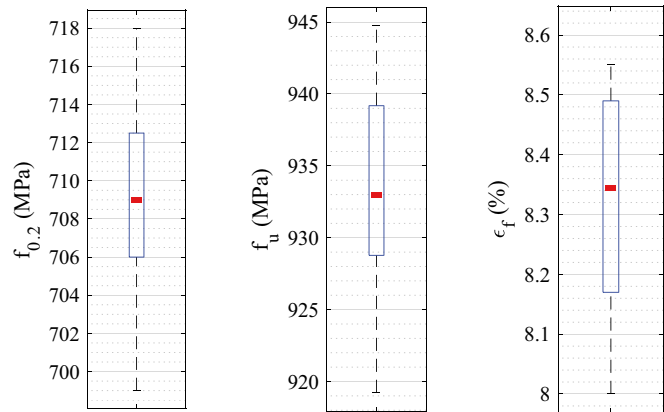
**Fig. 12** The 2D slices (thickness of  $0.2 \mu\text{m}$ ) extracted from R-RVE 1 in three orthogonal planes. The colors represent the grain ID in each grain which makes the colors shown in 2D slices different from those shown in the R-RVE



(a)



(b)



(c)

**Fig. 13** **a** Homogenized stress–strain curves from CP-FE simulations on R-RVE 1, SERVE 1, SERVE R1 to R8, and experimental test on Specimen 1; **b** variation of the relative error (%) of the predicted mechanical parameters with respect to the experimental values; and

**c** box plots (indicating the 25th and 75th percentiles) and mean values (red marker) of the predicted mechanical parameters predicted for SERVE R1 to R8

Further analysis was undertaken to understand the robustness of the three orthogonal 2D slices approach to extracting microstructural data. This was done by performing CP-FE simulations on additional SERVEs constructed from random orthogonal 2D slices extracted from the R-RVE created from Specimen 1 (i.e. R-RVE 1).

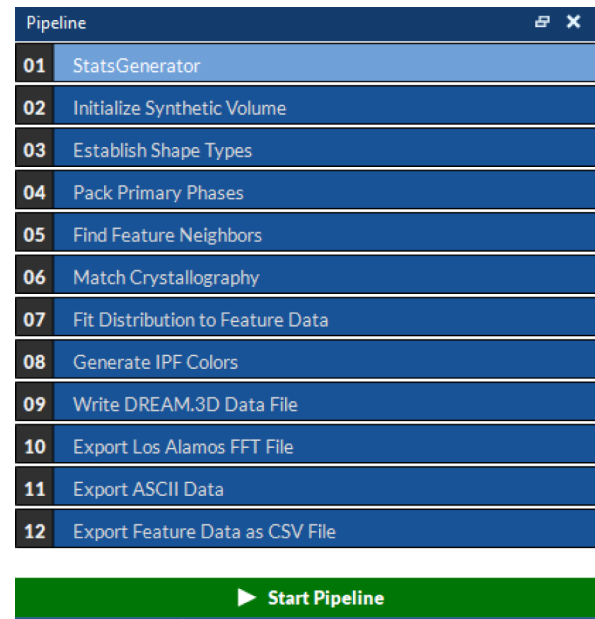
The following conclusions are drawn:

- Equivalence for predicting the homogenized tensile stress–strain curve of the L-PBF Ti–6Al–4V alloy using a CP-FE model was demonstrated between a SERVE generated from three orthogonal 2D EBSD scans and an R-RVE generated from multiple, parallel 2D EBSD scans collected by serial sectioning. The grain characteristics of the microstructure obtained from three orthogonal 2D EBSD scans results in the construction of SERVEs with close grain size and misorientation angle distributions as that extracted from the R-RVE.
- The predictive ability of the SERVE method was confirmed using additional SERVEs constructed from random combinations of orthogonal 2D slices extracted from the R-RVE.

## Appendix

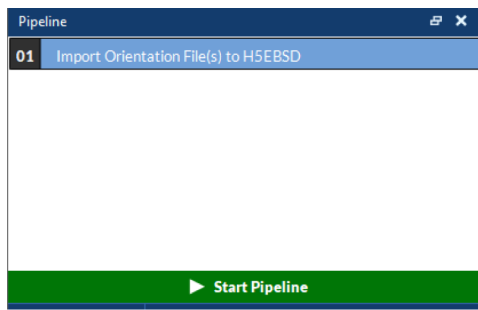
The customized pipelines used for construction of the SERVE and R-RVE in the DREAM.3D® software.

See Figs. 14 and 15.



(b) Step 2

Fig. 14 The pipelines used for construction of the SERVE



(a) Step 1



(b) Step 2

**Fig. 15** The pipelines used for construction of the R-RVE. The output of Step 1 (a) is input Pipeline 01 of Step 2 (b)

**Acknowledgements** This research is supported by the Commonwealth of Australia as represented by the Defence Science and Technology Group of the Department of Defence. The authors acknowledge the use of the instruments and the technical assistance of Dr Xi-Ya Fang at the Monash Centre for Electron Microscopy (a Node of Microscopy Australia) for the collection of the orthogonal EBSD images. The authors acknowledge the facilities, scientific, and technical assistance of Sydney Microscopy & Microanalysis (SMM), a University of Sydney Core Research Facility, and the University's Node of Microscopy Australia. In doing so, we particularly acknowledge Dr. Vijay Bhatia and Mr. Jacob Byrnes. The 3D EBSD data acquisition was sponsored by the Department of Industry, Innovation and Science under the auspices of the AUSMURI program.

**Funding** Open Access funding enabled and organized by CAUL and its Member Institutions.

**Open Access** This article is licensed under a Creative Commons Attribution 4.0 International License, which permits use, sharing, adaptation, distribution and reproduction in any medium or format, as long as you give appropriate credit to the original author(s) and the source, provide a link to the Creative Commons licence, and indicate if changes were made. The images or other third party material in this article are included in the article's Creative Commons licence, unless indicated otherwise in a credit line to the material. If material is not included in the article's Creative Commons licence and your intended use is not permitted by statutory regulation or exceeds the permitted use, you will need to obtain permission directly from the copyright holder. To view a copy of this licence, visit <http://creativecommons.org/licenses/by/4.0/>.

## References

- Azhari F et al (2022) Predicting the complete tensile properties of additively manufactured Ti-6Al-4V by integrating three-dimensional microstructure statistics with a crystal plasticity model. *Int J Plast* 148:103127
- Dawson PR, Boyce DE (2015) FE<sub>p</sub>X—finite element polycrystals: theory, finite element formulation, numerical implementation and illustrative examples. arXiv:1504.03296
- Shahba A, Ghosh S (2016) Crystal plasticity FE modeling of Ti alloys for a range of strain-rates: Part I: A unified constitutive model and flow rule. *Int J Plast* 87:48–68
- Ghosh S et al (2016) Crystal plasticity FE modeling of Ti alloys for a range of strain-rates: part II: Image-based model with experimental validation. *Int J Plast* 87:69–85
- Goh C-H, Neu RW, McDowell DL (2003) Crystallographic plasticity in fretting of Ti-6Al-4V. *Int J Plast* 19(10):1627–1650
- Mayeur JR, McDowell DL (2007) A three-dimensional crystal plasticity model for duplex Ti-6Al-4V. *Int J Plast* 23(9):1457–1485
- Mayeur JR, McDowell DL, Neu RW (2008) Crystal plasticity simulations of fretting of Ti-6Al-4V in partial slip regime considering effects of texture. *Comput Mater Sci* 41(3):356–365
- Zhang M, Zhang J, McDowell DL (2007) Microstructure-based crystal plasticity modeling of cyclic deformation of Ti-6Al-4V. *Int J Plast* 23(8):1328–1348
- Moore JA, et al (2017) Crystal plasticity modeling of  $\alpha/\beta$  phase deformation in Ti-6Al-4V. *Model Simul Mater Sci Eng* 25(7):075007
- Kasemer M, Quey R, Dawson P (2017) The influence of mechanical constraints introduced by  $\beta$  annealed microstructures on the yield strength and ductility of Ti-6Al-4V. *J Mech Phys Solids* 103:179–198
- Stopka KS, McDowell DL (2020) Microstructure-sensitive computational multi-axial fatigue of Al 7075-T6 and duplex Ti-6Al-4V. *Int J Fatigue* 133:105460
- Xiong Y et al (2020) Cold creep of titanium: Analysis of stress relaxation using synchrotron diffraction and crystal plasticity simulations. *Acta Mater* 199:561–577
- Zhang J, et al (2020) A multi-scale MCCPFEM framework: modeling of thermal interface grooving and deformation anisotropy of titanium alloy with lamellar colony. *Int J Plast* 135:102804
- Kapoor K et al (2018) Incorporating grain-level residual stresses and validating a crystal plasticity model of a two-phase Ti-6Al-4V alloy produced via additive manufacturing. *J Mech Phys Solids* 121:447–462
- Hu D, et al (2020) An anisotropic mesoscale model of fatigue failure in a titanium alloy containing duplex microstructure and hard  $\alpha$  inclusions. *Mater Des* 193:108844
- Asim UB, Siddiq MA, Kartal ME (2019) Representative volume element (RVE) based crystal plasticity study of void growth on phase boundary in titanium alloys. *Comput Mater Sci* 161:346–350
- Asim UB, Siddiq MA, Kartal ME (2019) A CPFEM based study to understand the void growth in high strength dual-phase titanium alloy (Ti-10V-2Fe-3Al). *Int J Plast* 122:188–211
- Liu J et al (2018) A three-dimensional multi-scale polycrystalline plasticity model coupled with damage for pure Ti with harmonic structure design. *Int J Plast* 100:192–207
- Ozturk D et al (2019) Two-way multi-scaling for predicting fatigue crack nucleation in titanium alloys using parametrically homogenized constitutive models. *J Mech Phys Solids* 128:181–207
- Kotha S, Ozturk D, Ghosh S (2019) Parametrically homogenized constitutive models (PHCMs) from micromechanical crystal plasticity FE simulations, part I: sensitivity analysis and parameter identification for Titanium alloys. *Int J Plast* 120:296–319
- Kotha S, Ozturk D, Ghosh S (2019) Parametrically homogenized constitutive models (PHCMs) from micromechanical crystal plasticity FE simulations: part II: Thermo-elasto-plastic model with experimental validation for titanium alloys. *Int J Plast* 120:320–339
- Kale C et al (2019) Oxygen effects on crystal plasticity of Titanium: A multiscale calibration and validation framework. *Acta Mater* 176:19–32
- Wang X et al (2019) A 3D crystal plasticity model of monotonic and cyclic simple shear deformation for commercial-purity polycrystalline Ti with a harmonic structure. *Mech Mater* 128:117–128
- Chatterjee K et al (2018) Prediction of tensile stiffness and strength of Ti-6Al-4V using instantiated volume elements and crystal plasticity. *Acta Mater* 157:21–32
- Kasemer M et al (2017) On slip initiation in equiaxed  $\alpha/\beta$  Ti-6Al-4V. *Acta Mater* 136:288–302
- Bažant ZP, Oh BH (1983) Crack band theory for fracture of concrete. *Matériaux et Construction* 16(3):155–177
- Swaminathan S, Ghosh S, Pagano NJ (2005) Statistically equivalent representative volume elements for unidirectional composite microstructures: part I - without damage. *J Compos Mater* 40(7):583–604
- Groerber M et al (2008) A framework for automated analysis and simulation of 3D polycrystalline microstructures. Part 2: Synthetic structure generation. *Acta Mater* 56(6):1274–1287
- Bagri A et al (2018) Microstructure and property-based statistically equivalent representative volume elements for polycrystalline Ni-based superalloys containing annealing twins. *Metall Mater Trans A* 49(11):5727–5744

30. Tucker JC et al (2012) Comparison of grain size distributions in a Ni-based superalloy in three and two dimensions using the Saltykov method. *Scripta Mater* 66(8):554–557
31. Lognormal distribution In: *Statistical Distributions*. pp 131–134 (2010)
32. Hutchinson JW (1976) Bounds and self-consistent estimates for creep of polycrystalline materials. *Proc R Soc Lond Ser A Math Phys Sci* 348(1652):101–127
33. Roters F et al (2010) Overview of constitutive laws, kinematics, homogenization and multiscale methods in crystal plasticity finite-element modeling: Theory, experiments, applications. *Acta Mater* 58(4):1152–1211
34. Peirce D, Asaro RJ, Needleman A (1983) Material rate dependence and localized deformation in crystalline solids. *Acta Metall* 31(12):1951–1976
35. Asaro RJ (1983) Crystal Plasticity. *J Appl Mech* 50(4b):921–934
36. Smith WF, Hashemi J (2005) *Foundations of materials science and engineering*. McGraw-Hill, Boston
37. Kim J-B, Yoon JW (2015) Necking behavior of AA 6022–T4 based on the crystal plasticity and damage models. *Int J Plast* 73:3–23
38. Huang Y (1991) A user-material subroutine incorporating single crystal plasticity in the ABAQUS finite element program. Division of Applied Sciences, Harvard University
39. ABAQUS/Standard (2017) Dassault Systèmes Simulia Corp.
40. Verma RK, Biswas P (2016) Crystal plasticity-based modeling of grain size effects in dual phase steel. *Mater Sci Technol* 32(15):1553–1558
41. Naderi M et al (2016) Prediction of fatigue crack nucleation life in polycrystalline AA7075-T651 using energy approach. *Fatigue Fract Eng Mater Struct* 39(2):167–179
42. Kashinga RJ et al (2017) Low cycle fatigue of a directionally solidified nickel-based superalloy: testing, characterisation and modelling. *Mater Sci Eng, A* 708:503–513
43. Nye JF (1972) *Physical properties of crystals: their representation by tensors and matrices*. Clarendon Press
44. Abbassi F et al (2015) FE simulation and full-field strain measurements to evaluate the necking phenomena. *Procedia Manufacturing* 2:500–504
45. Dutoit SHC (2012) *Graphical exploratory data analysis*. Springer

**Publisher's Note** Springer Nature remains neutral with regard to jurisdictional claims in published maps and institutional affiliations.